MIT Open Access Articles

A Systematic Approach to Modeling Impedances and Current Distribution in Planar Magnetics

Citation	Chen, Minjie, Mohammad Araghchini, Khurram K. Afridi, Jeffrey H. Lang, Charles R. Sullivan, and David J. Perreault. "A Systematic Approach to Modeling Impedances and Current Distribution in Planar Magnetics." The 2014 IEEE Workshop on Control and Modeling for Power Electronics, June 2014.
As Published	http://www.ieee-compel.org/files/2014/07/Program2.pdf
Publisher	Institute of Electrical and Electronics Engineers (IEEE)
Version	Author's final manuscript
Citable link	http://hdl.handle.net/1721.1/89430
Terms of Use	Creative Commons Attribution-Noncommercial-Share Alike
Detailed Terms	http://creativecommons.org/licenses/by-nc-sa/4.0/

A Systematic Approach to Modeling Impedances and Current Distribution in Planar Magnetics

Minjie Chen[†], Mohammad Araghchini[†], Khurram K. Afridi[‡], Jeffrey H. Lang[†],
Charles R. Sullivan[§] and David J. Perreault[†]

[†]Massachusetts Institute of Technology, Cambridge, Massachusetts, 02139, USA
[‡]University of Colorado at Boulder, Boulder, Colorado, 80309, USA
[§]Dartmouth College, Hanover, New Hampshire, 03755, USA
Email: minjie@mit.edu

Abstract—**Planar magnetic components using printed-circuit-board windings are attractive due to their high repeatability, good thermal performance and usefulness for realizing intricate winding patterns. To enable higher system integration at high switching frequency, more sophisticated methods that can rapidly and accurately model planar magnetics are needed. This paper develops a lumped circuit model that captures the impact of skin and proximity effects on current distribution and electromagnetic fields in planar magnetics. This enables accurate predictions of impedances, losses, stored reactive energy and current sharing among parallel windings. This lumped model is also a circuit domain representation of electromagnetic interactions. It can be used to simulate circuits incorporating planar magnetics, to visualize the electromagnetic fields, and to extract parameters for magnetic models by simulations. The modeling results match with previous theories and finite-element-modeling results. A group of planar magnetic devices, including transformers and inductors with various winding patterns, are prototyped and measured to validate the proposed approach.**

I. Introduction

For inductors and transformers in high-frequency power conversion applications, windings fabricated in a printed-circuit-board process with ferrite cores assembled through holes in the board have become a popular strategy. We use the term *planar magnetics* for this approach, which offers high repeatability, good thermal performance, and the ease of realizing intricate winding patterns [1]–[4]. These advantages makes planar magnetics attractive as switching frequencies increase [5]–[7]. However, the increasing skin and proximity effects and the resulted self and mutual impedances make the modeling challenging, especially when parallel windings are included. Previous modeling efforts have estimated ac resistance [8]–[12], predicted parasitics [13]–[15], estimated core losses [16]–[21], generated circuit representations [22], [23], extracted parameters by experimental measurements [24], [25], developed transmission line models [26], [27], [29]–[31], and investigated current sharing among parallel and interleaved windings [32]–[35]. These approaches have different focuses, rely on various assumptions, and sometimes are not easy to use. Numerical methods (e.g., finite-element-modeling (FEM)) and experimental measurements are widely applicable, but are time-consuming, not analytical and difficult to use for design optimization. A systematic approach to modeling planar magnetics, which is analytical with low computational

requirements, and capable of capturing many parameters under a unified setup, is needed and is the main focus of this paper.

Models for planar magnetics commonly share two assumptions, in addition to other case-by-case assumptions. The first common assumption is the "1-D assumption", under which the electromagnetic field and current distribution within the winding change only along the thickness of the winding. This assumption is satisfied in many designs using high-permeability cores. The second assumption is the "MQS assumption": the electromagnetic field in the planar structure satisfies the Magneto-Quasi-Static (MQS) requirements [36], [37], in which the time derivative of the electric field (i.e. capacitive effect) can be decoupled from the other terms in Maxwell's equations and modeled separately with other specific approaches. In a majority of power electronics applications, the MQS assumption is satisfied.

This paper presents a systematic approach to modeling planar magnetics under these two assumptions. The electromagnetic interactions within and among the windings of a planar structure are expressed using the MQS version of Maxwell's equations. These equations are converted into a lumped circuit model with frequency dependent element values. The lumped circuit model bridges the circuit domain and the electromagnetic domain: it allows the electromagnetic field and current distributions to be easily determined with very low computational requirements, provides insights into the magnetic structure design, and is useful for modeling circuits incorporating planar magnetic devices. The modeling approach is applicable to a wide variety of devices, from inductors and coupled inductors to multiple-winding transformers incorporating interleaving among windings, paralleled windings and energy storage (e.g., for flyback transformers). Alternatively, for a given frequency, this lumped model can be solved by circuit simulators (e.g. SPICE). With some modifications, the lumped circuit is also capable of capturing wide frequency range operation, such as for use in time-domain simulations. The proposed approach can be applied to various applications, from windings in planar transformers to windings in machines.

The remainder of the paper is organized as follows. Section II outlines the terminology used in this paper, and presents an overview of the proposed approach. A step-by-step derivation of the lumped circuit model is provided in Section III.
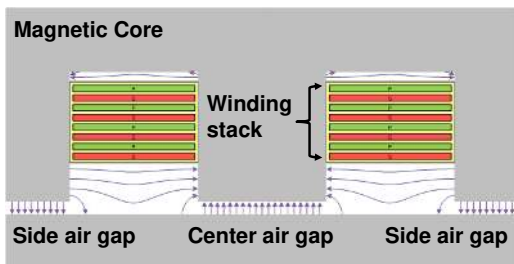
Fig. 1. Cross-sectional view of a planar magnetic structure. It comprises a magnetic core, a winding stack and a set of possible air gaps.
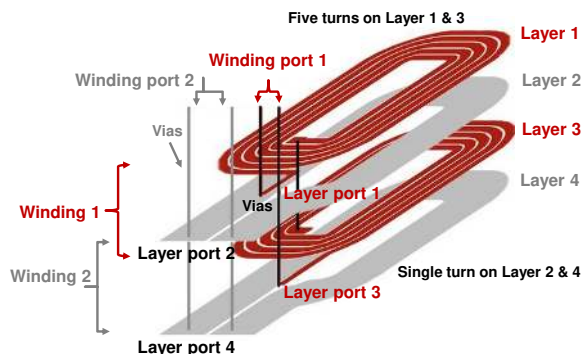

Fig. 2. Winding stack of an example two-winding, four-layer transformer with 10:1 turns ratio.

Section IV explains how the lumped circuit model can be applied in circuit simulations, field visualizations and parameter extractions. The proposed approach is verified through FEM simulations and experimental measurements in Section V. Section VI investigates a few practical design constraints, and quantitatively shows the performance of this approach under these constraints. Finally, Section VII summarizes the paper. A detailed derivation of the lumped circuit model is provided in Appendix I, while Appendix II presents theoretical verifications of the proposed approach by comparing it with existing models and theories.

II. OVERVIEW OF THE APPROACH

The terminology used in this paper is illustrated in Fig. 1 and Fig. 2. As shown in Fig. 1, a planar magnetic structure comprises a **winding stack**, a **magnetic core**, and a set of possible **air gaps**. A winding stack has one or more **windings**. Each winding comprises one or more turns on one or more **layers**. Each layer can have multiple **turns** as shown in Fig. 2. Usually, turns on the same layer are connected in series. Each layer has a **layer port**. Layer ports are connected by **electrical vias** to form windings. Turns on different layers can be connected in series or parallel, and can be interleaved in various ways. An example winding stack with two windings and a $10:1$ primary-to-secondary turns ratio is shown in Fig. 2. It has four layers: layer 1 and layer 3 each have five turns and are connected in series; layer 2 and layer 4 each have a single turn and are connected in parallel.

The core of this approach is a lumped circuit model. Using

a lumped circuit to model planar magnetics is not new. Here we highlight two branches of previous work to provide the background and clarify the differences between the modeling approach presented in this paper with those in the literature.

Keradec and colleagues modeled multilayer windings in a magnetic component by adapting models for electromagnetic waves propagating in multilayered media, as is sometimes found in optical systems [22], [23], [25], [33], [34]. Analogies were made between the circuit domain and the optic domain. This model is simple, analytical and intuitive. However, it requires unwieldy assumptions for the analogies to be fully satisfied. Additional analogies are needed to make the model applicable to more sophisticated cases. Nevertheless, this set of papers introduces a valuable framework for mapping electromagnetic relationships among layers into connections of two-port circuit blocks, an approach we also adopt (albeit modified for our model). Lopera and colleagues also developed models to capture the behavior of magnetic components of multilayer magnetic windings. To capture the effects of electromagnetic fields diffusing through conductors, the authors introduce a lossy transmission line model for each layer, and interconnect the transmission-line structures to model the whole magnetic component [26]–[31]. The behavior of the resulting system is found using numerical methods (e.g., with a circuit simulator), essentially placing the burden of solving for the electromagnetic response onto the circuit simulator. This approach is comparable to finite-element approaches (but with relatively fast solution) and can naturally capture 2-D cases [28]. Moreover, the bandwidth of the model is limited only by the resolution of the discretization of conductor layers. If this discretization is fine enough to accurately capture behavior at the maximum frequency of interest, the model can be used for time-domain simulations as well as frequency-domain simulations.

The modeling approach presented in this paper has the advantages of (1) being developed directly from basic electromagnetic theories, which allows it to be easily interpreted and rapidly implemented, (2) providing simple, computationally-efficient analytical solutions with clear boundaries of applicability. The circuit architecture and element values in the model are entirely determined by Maxwell's equations and do not need to rely upon intuitive judgments/selections. In this sense the proposed model takes on the best characteristics of each of the above-described approaches. It is particularly effective and efficient when one seeks frequency-domain representation of magnetic component behavior (e.g., an impedance matrix description of a component). This approach represents a new way of systematically interpreting the electromagnetic interactions in planar magnetics, and is organized and presented with focus on practical usefulness for circuit designers.

The modeling approach begins by developing an impedance network model for a single turn on a layer (referred to here as a one-turn layer). This network model is repeated and extended to model multiple layers with multiple turns. The magnetic core, the air gaps and the cross-layer connections (electrical vias) place additional boundary conditions on the impedance
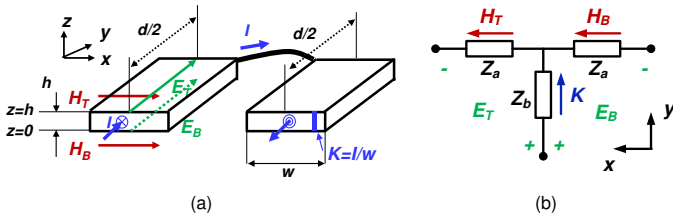
Fig. 3. (a) a one-turn layer and (b) its three-terminal impedance network. The x and y axes indicate the defined positive direction of the H field and E field, respectively. A positive $E|H$ field in the physical structure is represented by a positive $E|H$ value in the impedance network. The two conductors form a single turn and are connected by a interconnect wire whose impedance is neglected. This single-turn is modeled as a three terminal impedance network.

networks, and are modeled by additional components in the lumped model. To make the magnetic model compatible with circuit domain analysis, linear conversions (modeled using dependent sources and ideal transformers) and electrical interconnects are used to link the electromagnetic domain to the circuit domain.

III. GENERATING THE LUMPED CIRCUIT MODEL

A. Modeling a one-turn layer.

Fig. 3a shows the geometry of a one-turn layer, with length d, width w, and thickness h. This single turn is driven (or loaded) by an external current I (having integrated surface current density, current per width, K with units "A/m"), inducing a voltage V across its two terminals. $H_T|H_B$ is the magnetic field (H field) strength on the top|bottom surface of the layer (along the width). $E_T|E_B$ is the electric field (E field) strength on the top|bottom surface of the layer (along the length). As will be derived in Appendix I, solving the 1-D diffusion equation in the conductor, with the specified boundary conditions [37], and applying Ohm's Law ($J = \sigma E$; where σ is the conductivity of this conductor) gives the relationship between the magnetic fields and electric fields on the top and bottom surfaces, and the integrated surface current density K carried by this layer:

$$
\begin{aligned}
E_T &= Z_a \ H_T + Z_b \ K \\
\underbrace{E_B}_{\text{V/m}} &= \underbrace{Z_b}_{\Omega} \underbrace{K}_{A/m} - \underbrace{Z_a}_{\Omega} \underbrace{H_B}_{A/m}.
\end{aligned} \tag{1}
$$

Here Z_a and Z_b are two complex impedances (with units of Ω) determined by the geometry of the structure and the operating angular frequency (ω), and are given by

$$
\begin{aligned}
Z_a &= \frac{\Psi(1 - e^{-\Psi h})}{\sigma(1 + e^{-\Psi h})} \\
Z_b &= \frac{2\Psi e^{-\Psi h}}{\sigma(1 - e^{-2\Psi h})}.
\end{aligned} \tag{2}
$$

Here $\Psi = \frac{1+j}{\delta}$, where $\delta = \sqrt{\frac{2}{\mu\omega\sigma}}$ is the skin depth of the conductor and μ is its permeability of this conductor. Note that all variables (E, H, V, I, Z, etc.) are complex variables. Also, H_T, H_B, I and K are related through Ampere's law:

$$
(H_T - H_B)w = I = Kw. \tag{3}
$$

Since H_T, H_B, and K are related to current (with units of A/m), E_T and E_B are related to voltage (with units of V/m), and Z_a and Z_b are impedances (with units of Ω), (1) and (3) can be considered as the KVL and KCL functions of a three-terminal impedance network, as shown in Fig. 3b. This result is similar to the circuit structure in [14] and references therein, albeit with different assumptions and interpretations about the nature and propagation of the fields.

B. Modeling two adjacent layers.

Figure 4a shows the geometry of two adjacent one-turn layers separated by a spacing (created with an insulator) between them. Based on the previous subsection, the electromagnetic fields around and within each layer can be described by the following two sets of equations

Layer 1: Layer 2:

$$
\begin{cases}
E_{T1} = Z_{a1}H_{T1} + Z_{b1}K_1 \\
E_{B1} = Z_{b1}K_1 - Z_{a1}H_{B1} \\
H_{T1} - H_{B1} = K_1 \\
wK_1 = I_1.
\end{cases}
\qquad
\begin{cases}
E_{T2} = Z_{a2}H_{T2} + Z_{b2}K_2 \\
E_{B2} = Z_{b2}K_2 - Z_{a2}H_{B2} \\
H_{T2} - H_{B2} = K_2 \\
wK_2 = I_2.
\end{cases}
\tag{4}
$$

Here $H_{Ti}|H_{Bi}$ is the magnetic field strength on the top|bottom surface of the layer i; $E_{Ti}|E_{Bi}$ is the electric field strength on the top|bottom surface of layer i; Z_{ai} and Z_{bi} are complex impedances of layer i defined by the geometry and frequency; I_i is the current that is carried by layer i. Based on (4), layer 1 and layer 2 can be represented by two three-terminal impedance networks labeled as "Layer 1" and "Layer 2" in Fig. 4b. Also labeled are the associated electromagnetic field variables on the top and bottom surfaces of each layer.

The electromagnetic fields surrounding the two layers are related by the magnetic flux flowing between them (Φ_{S12}). The spacing has a thickness a_1, width w and length d. From flux continuity, the magnetic field strength in the spacing, H_{S12}, equals H_{B1} and H_{T2}. Considering the voltage loops on the bottom surface of layer 1, and on the top surface of layer 2 (including layer surfaces, external wires and sources surrounding the center post), and using Faraday's law and flux continuity (as shown in Appendix I), the magnetic flux flowing through the center post across the two surfaces, Φ_{B1} and Φ_{T2}, can be written as functions of the electric fields on the two layer surfaces (E_{B1}, E_{T2}), as well as the external voltages applied to the two layer ports (V_1 and V_2), such that

$$
\begin{cases}
j\omega\Phi_{B1} = V_1 - dE_{B1} \\
j\omega\Phi_{T2} = V_2 - dE_{T2} \\
\Phi_{B1} + \Phi_{S12} = \Phi_{T2} \\
H_{S12} = \frac{\Phi_{S12}}{\mu_0 a_1 d}.
\end{cases}
\tag{5}
$$

Here the permeability of the space (insulator) between the two layers is assumed to be μ_0. From Fig. 5, the magnetic field H_{S12} can be expressed as
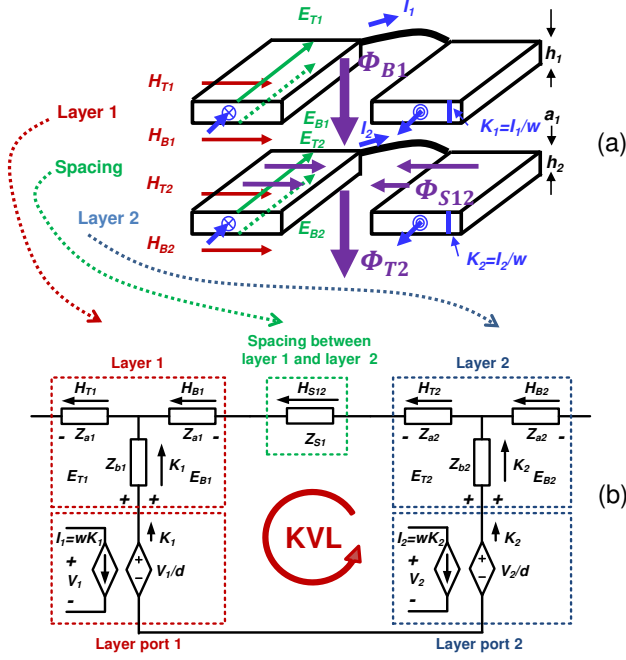
Fig. 4. Two one-turn adjacent layers: (a) geometry and (b) impedance network model with "V/m", "A/m" and "Ω" as the internal units. The variables within the voltage dependent voltage sources are H, E and K and are in the electromagnetic domain. The variables outside the current dependent current sources are voltages and currents and are in the circuit domain.
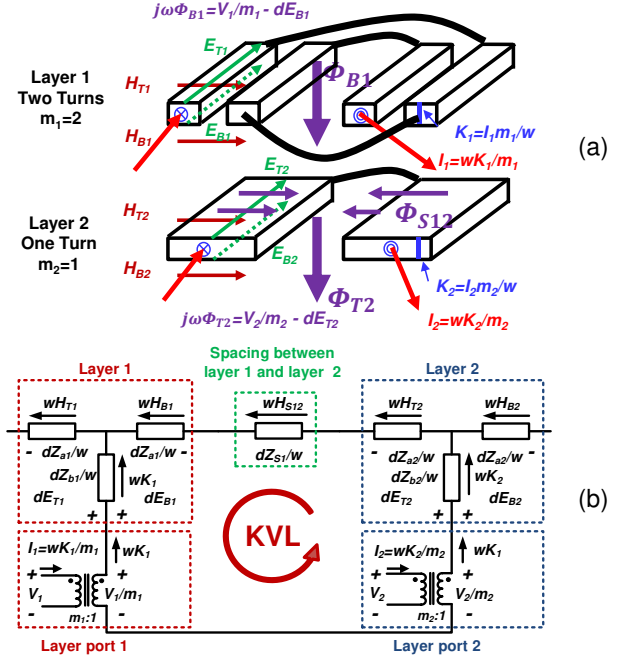

Fig. 5. Two adjacent layers - one layer with a single turn, and the other layer with two series-connected turns: (a) geometry and (b) impedance network model with "V", "A", and "Ω" as the internal units. This system is entirely in the circuit domain. Skin and proximity effects are captured by using the complex impedances determined by solutions to 1-D diffusion equations.

$$H_{S12} = \frac{1}{j\omega\mu_0 a_1} \left(\frac{V_2}{d} - E_{T2} - \frac{V_1}{d} + E_{B1} \right). \qquad (6)$$

Defining $Z_{S1} = j\omega\mu_0 a_1$ gives

$$\underbrace{H_{S12}}_{\text{A/m}} \underbrace{Z_{S1}}_{\Omega} = \underbrace{\frac{V_2}{d} - E_{T2} - \frac{V_1}{d} + E_{B1}}_{\text{V/m}}. \qquad (7)$$

Eq. (7) may be thought of as a KVL relation that links the two impedance networks. The resulting lumped circuit model for two adjacent layers is shown in Fig. 4b. Note that the integrated surface current densities, K_1 and K_2, need to be linearly converted into external layer currents $I_1 = wK_1$ and $I_2 = wK_2$. These linear conversions are modeled with current-dependent-current-sources (CDCS) with gains of w (layer width). According to (7), linear conversions are also required to convert the induced layer port voltages V_1 and V_2 to $\frac{V_1}{d}$ and $\frac{V_2}{d}$. These linear conversions are modeled with voltage-dependent-voltage-sources (VDVS) with gains of $\frac{1}{d}$. These VDVSs and CDCSs are paired up for each layer and labeled as "layer ports" in Fig. 4b.

If there are m_i series-connected turns on layer i, and all turns have the same width - $\frac{w}{m_i}$, thickness - h_i and length - d, H_{Ti}, H_{Bi} and K_i are linearly related to I_i: $I_i = \frac{wK_i}{m_i} = \frac{w(H_{Ti}-H_{Bi})}{m_i}$. Also Φ_i is linearly related to E_i and V_i: $j\omega\Phi_i = \frac{V_i}{m_i} - dE_i$. Figure 5a shows an example setup with layer 1 having two series-connected turns, and layer 2 having a single turn. Assuming layer 1 has m_1 turns ($m_1 = 2$), and layer 2

has m_2 turns ($m_2 = 1$), (4) and (7), which are interchangeable with the lumped circuit model of Fig. 4b, generalize to

$$
\text{Layer 1}: \begin{cases} \underbrace{dE_{T1}}_{\text{V}} = \underbrace{wH_{T1}}_{\text{A}} \underbrace{\frac{d}{w}Z_{a1}}_{\Omega} + \underbrace{wK_1}_{\text{A}} \underbrace{\frac{d}{w}Z_{b1}}_{\Omega} \\ dE_{B1} = wK_1\frac{d}{w}Z_{b1} - wH_{B1}\frac{d}{w}Z_{a1} \\ H_{T1} - H_{B1} = K_1 \\ wK_1 = I_1 m_1. \end{cases}
$$

$$
\text{Layer 2}: \begin{cases} dE_{T2} = wH_{T2}\frac{d}{w}Z_{a2} + wK_2\frac{d}{w}Z_{b2} \\ dE_{B2} = wK_2\frac{d}{w}Z_{b2} - wH_{B2}\frac{d}{w}Z_{a2} \\ H_{T2} - H_{B2} = K_2 \\ wK_2 = I_2 m_2. \end{cases} \qquad (8)
$$

$$
\text{Spacing}: \underbrace{\frac{V_2}{m_2} - dE_{T2} - \frac{V_1}{m_1} + dE_{B1}}_{\text{V}} = \underbrace{wH_{S12}}_{\text{A}} \underbrace{\frac{d}{w}Z_{S1}}_{\Omega}.
$$

This set of equations is expressed with individual terms having units of "V", "A" or "Ω". It can be represented by a clarified lumped circuit model as shown in Fig. 5b. All impedances are linearly scaled up with a geometry factor of $\frac{d}{w}$. The CDCSs and VDVSs are replaced by ideal transformers with turns ratios of m_1 and m_2, representing the numbers of physical turns on each layer. With these linear conversions, all variables in the system of Fig. 5 is entirely in the circuit domain.
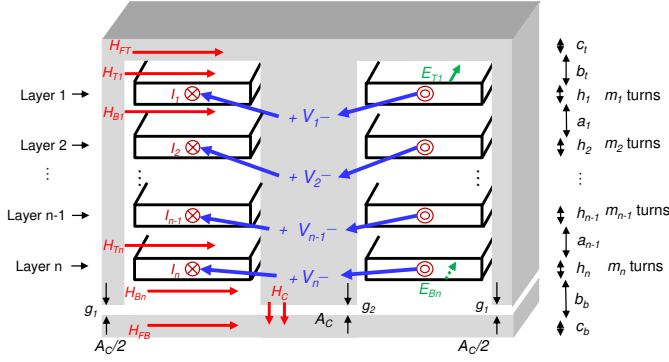
Fig. 6. Planar structure with n layers, a magnetic core and multiple air gaps, with $g_1 + g_2$ as the total gap length. All layers are drawn as one-turn layers for simplicity. In a general case, layer 1 to layer n have m_1 to m_n series-connected turns, respectively. The m_i series-connected turns on layer i have the same width - w/m_i, thickness - h_i, and length - d.

C. Modeling layer stacks with a magnetic core and multiple air gaps

To complete the model, consider a planar structure with n layers, a magnetic core and two air gaps as shown in Fig. 6. The number of series-connected turns on layer 1 to layer n are m_1 to m_n, respectively. The core has a gap of length g_1 in the outer surface, and a gap of length g_2 in the center post (the total length of the air gap is $g_1 + g_2$). The cross sectional area of the air gap in the center post is A_c and in the outer surface is $\frac{A_c}{2}$. The thicknesses of layers 1 to n are h_1 to h_n, respectively. The spacing thickness between layer i and layer $(i+1)$ is a_i. The spacing thickness between the top surface of layer 1 and the magnetic core is b_t. The spacing thickness between the bottom surface of layer n and the magnetic core is b_b. The thickness of the top core layer is c_t; the thickness of the bottom core layer is c_b. The magnetic field strength on the top|bottom surface of the layer i is $H_{Ti}|H_{Bi}$. The electric field strength on the top|bottom surface of layer i is $E_{Ti}|E_{Bi}$. The external voltages that are applied to layers 1 to n are V_1 to V_n, respectively. The currents that flow through layers 1 to n are I_1 to I_n, respectively.

We investigate how these variables are related. The lumped model for the n layers are generated by simply repeating the lumped model of two adjacent layers (repeating (8) and Fig. 5). The magnetic core and the air gaps impose additional boundary conditions, and hence add additional circuit elements. Using Maxwell's equations and flux continuity, as shown in Appendix I, the variables on the top side of the layer stack, E_{T1}, H_{T1}, m_1 and V_1, are related by

$$dE_{T1} - \frac{V_1}{m_1} = -\frac{d}{w}j\omega\mu_r\mu_0 c_t w H_{T1} - \frac{d}{w}j\omega\mu_0 b_t w H_{T1}. \quad (9)$$

Similarly, neglecting air-gap fringing, the variables on the bottom side of the layer stack, E_{Bn}, H_{Bn}, m_n and V_n, are related by

$$dE_{Bn} - \frac{V_n}{m_n} = \frac{d}{w}j\omega\frac{w\mu_0 A_c}{d(g_1 + g_2 + \frac{A_c w}{\mu_r c_b d})}wH_{Bn} + \frac{d}{w}j\omega\mu_0 b_b w H_{Bn}. \quad (10)$$

Defining the following four impedances:

$$\begin{aligned} Z_{tf} &= j\omega\mu_r\mu_0 c_t \\ Z_{ts} &= j\omega\mu_0 b_t \\ Z_{bf} &= j\omega\frac{w\mu_0 A_c}{d(g_1 + g_2 + \frac{A_c w}{\mu_r c_b d})} \\ Z_{bs} &= j\omega\mu_0 b_b, \end{aligned} \quad (11)$$

Eq. (9) and (10) can be rewritten as

$$\begin{aligned} dE_{T1} - \frac{V_1}{m_1} &= -wH_{T1}(\frac{d}{w}Z_{tf} + \frac{d}{w}Z_{ts}) \\ dE_{Bn} - \frac{V_n}{m_n} &= wH_{Bn}(\frac{d}{w}Z_{bf} + \frac{d}{w}Z_{bs}). \end{aligned} \quad (12)$$

Eq. (12) represents additional boundary conditions that supplement the equations given by (8). They are modeled with four additional impedances ($\frac{d}{w}Z_{tf}$, $\frac{d}{w}Z_{ts}$, $\frac{d}{w}Z_{bf}$ and $\frac{d}{w}Z_{bs}$) in Fig. 7, which is the full lumped circuit model for the planar structure of Fig. 6. The impedance networks representing layers 1 to n are simple repetitions of the impedance network shown in Fig. 5b. The impedances Z_{ts} and Z_{tf} on the left side represent the spacing and the magnetic core above the layer stack. The Z_{bs} and Z_{bf} on the right side represent the spacing, the magnetic core, and the air gaps below the layer stack. All impedances (Z_{ai}, Z_{bi}, Z_{Si}, Z_{tf}, Z_{ts}, Z_{bf}, Z_{bs}) are scaled up by $\frac{d}{w}$ to account for the geometry of the structure, placing the model in the circuit domain.

The lumped circuit model shown in Fig. 7 is determined by, and is interchangeable with Maxwell's equations. All connections (circuit architecture) are strictly determined by KVL and KCL rules. All impedance values are calculated from the geometry of the planar structure and the operating frequency. All across and through variables (V_i, I_i, wH_{Bi}, wH_{Ti}, etc.) and parameters (m_i, d, w, h_i, etc.) have clear physical meanings. All units are compatible with circuit analysis and simulations (with units of "V", "A" and "Ω").

D. Modeling cross-layer connections (electrical vias)

In a planar structure, multiple layers are connected by cross-layer connections (electrical vias) to form complete windings. Layers can be interleaved in multiple ways. These electrical vias place additional constraints to the lumped circuit model, and can be realized by connecting the corresponding layer ports in the same pattern as they are connected in the physical circuit. For example, consider the case where layer i and layer j are connected in series to form winding a, driven by voltage V_a and carrying current I_a, and layer k and layer l are connected in parallel to form winding b, driven by voltage V_b and carrying net current I_b. The following four constraints

$$\begin{cases} V_i + V_j = V_a \\ V_k = V_l = V_b \\ I_i = I_j = I_a \\ I_k + I_l = I_b. \end{cases} \quad (13)$$
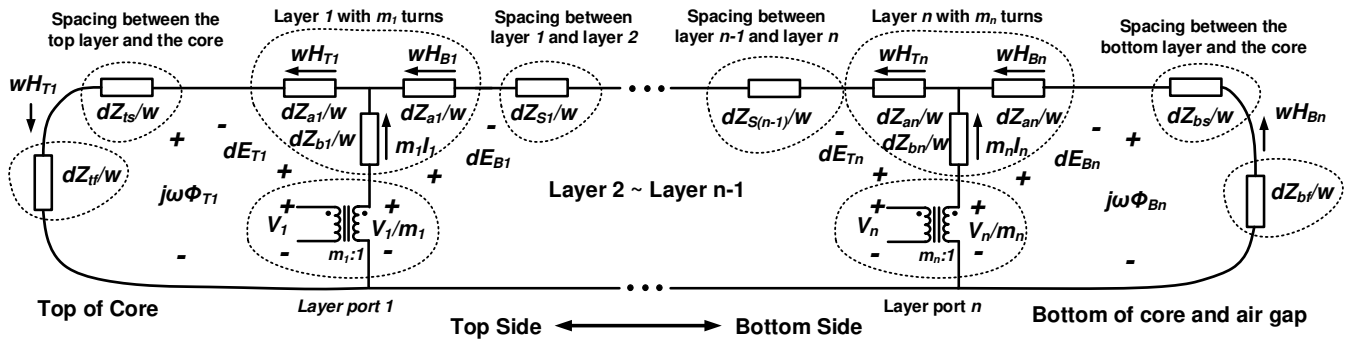
Fig. 7. Lumped circuit model for a planar magnetic structure with n windings, a magnetic core and air gaps as shown in Fig. 6. All layers have the same length - d and width - w. Layer 1 to layer n have m_1 to m_n series-connected turns, respectively. The m_i series-connected turns on layer i have the same width - w/m_i, thickness - h_i, and length - d.
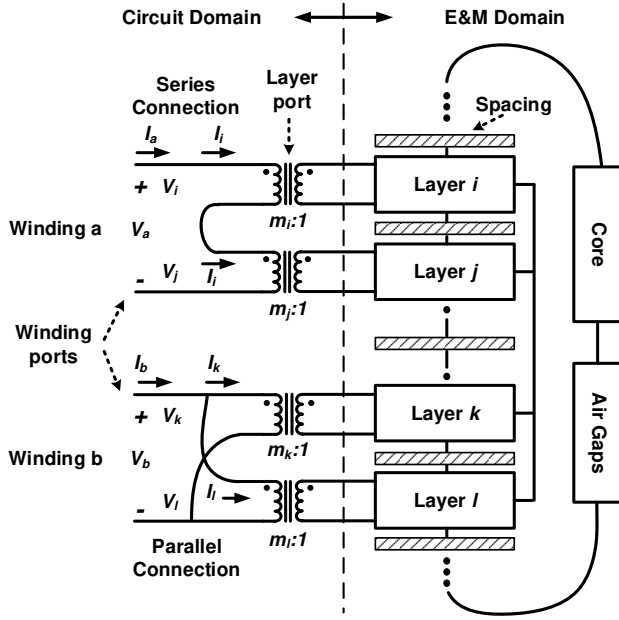

Fig. 8. Modeling cross-layer connections (electrical vias) of the layer ports to formulate windings. Layers i and j are connected in series, and layers k and l are connected in parallel.

are added to the existing Maxwell's equation sets ((8), and (12)). These constraints are included in the lumped circuit model by connecting the layer ports of layer i and layer j in series, and connecting the layer ports of layer k and layer l in parallel, as shown in Fig. 8.

E. Summary of the lumped circuit model

Here we summarize the method for generating the lumped circuit model. All variables are the same as previously defined.

1) Conductor layers: Each conductor layer i is modeled as a three-terminal impedance network comprising two impedances $\frac{d}{w}Z_{ai}$ and one $\frac{d}{w}Z_{bi}$. The values of Z_{ai} and Z_{bi} are determined by the thickness (h_i) of this layer, characteristics of the conductive material (μ_i, σ_i), the angular operating frequency (ω), $\Psi_i = \frac{1+j}{\delta_i}$, and $\delta_i = \sqrt{\frac{2}{\mu_i \omega \sigma_i}}$, according to

$$Z_{ai} = \frac{\Psi_i(1 - e^{-\Psi_i h_i})}{\sigma_i(1 + e^{-\Psi_i h_i})}$$
$$Z_{bi} = \frac{2\Psi_i e^{-\Psi_i h_i}}{\sigma_i(1 - e^{-2\Psi_i h_i})}. \tag{14}$$

The geometry factor of $\frac{d}{w}$ needs to be applied to all impedances to bring the result into the circuit domain. In a majority of planar structures which satisfy the "1-D assumption", all layers have the same length d and width w.

2) Layer ports: Each conductor layer has a layer port. It performs linear conversions, and allows connections to other layers through electrical vias. The interconnection into the electromagnetic model at the layer port is realized with an ideal transformer, whose turns ratio equals the number of series-connected turns on that layer ($m_i : 1$).

3) Spacings: The spacings between adjacent layers are modeled by impedances. The interconnect impedance between layer i and layer $(i+1)$ is $\frac{d}{w}Z_{Si}$, where

$$Z_{Si} = j\omega\mu_i a_i. \tag{15}$$

Here the spacing between layer i and layer $(i+1)$ has thickness of a_i and permeability of μ_i. The interconnect impedance between the top/bottom surfaces of the layer stack to the top/bottom side of the magnetic core is $\frac{d}{w}Z_{ts}$ and $\frac{d}{w}Z_{bs}$, where

$$Z_{ts} = j\omega\mu_0 b_t$$
$$Z_{bs} = j\omega\mu_0 b_b. \tag{16}$$

4) Magnetic core and air gaps: The magnetic core and air gaps are modeled by additional impedances. The impedance which represents the electromagnetic coupling at the top of the magnetic core (without the air gap) is $\frac{d}{w}Z_{tf}$, where

$$Z_{tf} = j\omega\mu_r\mu_0 c_t. \tag{17}$$

Here μ_r is the relative permeability of the core material. The impedance which represents the electromagnetic coupling at the bottom of the core (including the air gaps) is $\frac{d}{w}Z_{bf}$, where

$$Z_{bf} = j\omega\frac{w\mu_0 A_c}{d(g + \frac{A_c w}{\mu_r c_b d})}. \tag{18}$$
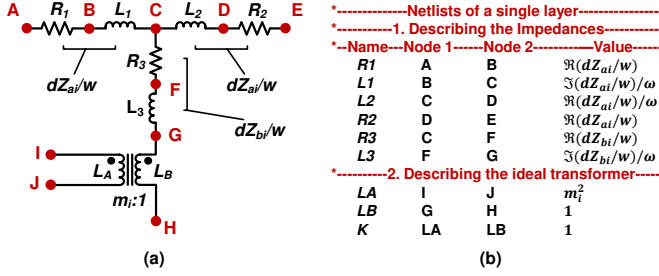
Fig. 9. Lumped circuit model and its netlist for a one-turn layer. Here $\Re$ represents the real part of a complex value, and $\Im$ represents the imaginary part of a complex value.

Here g is the total effective length of the air gaps.

5) Cross-layer connections (electrical vias): The final step is to connect the ideal transformers of the impedance networks of each layer in the same pattern as they are connected in the physical circuits.

IV. APPLICATIONS

A. Circuit simulation

At a single operating frequency, the lumped circuit model shown in Fig. 7 (and shown in Fig. 8 with cross-layer connections included) can be described by a netlist, and directly solved by circuit simulator, such as SPICE. For example, a layer with m_i series-connected turns can be represented by a lumped circuit model as shown in Fig. 9a, and described by a netlist as shown in Fig. 9b. Since the lumped circuit model is highly repetitive, the netlist for the full structure can be generated by simply repeating this network and modifying the impedance values. SPICE or similar simulations can be used to determine the current flowing through each winding and each layer, to calculate the magnetic field strengths at the surface of each conductor, and to perform small signal analysis between two ports. Since the impedance values are calculated using 1-D diffusion equations, this circuit simulation captures the skin and proximity effects, allowing impedances, losses, stored reactive energy, current sharing, etc., to be determined under a unified setup.

The model can be extended to be capable of modeling systems with wide frequency range by various known techniques. One is to simply repeat the modeling approach at each independent frequency of interest. The other is to generate more complicated impedance networks to capture behavior over a wide frequency range. Methods in this type include simple first- or second-order approximate networks [22], and discretized numerically-fitted networks [27]. Designers can make tradeoffs between model simplicity and accuracy by choosing and mixing these techniques.

B. Field Visualization

This model also provides insight into the design of the magnetic structure. Fields at the surface of conductors solved using the lumped circuit model (i.e. H_T, H_B and K) can be used in determining the fields and current densities inside the conductors using known formulations. For example, based on knowing the fields at the conductor surfaces and the 1-D diffusion equation (provided in Appendix I), the magnetic field distribution inside the conductor as a function of the distance from the surfaces can be found by

$$H_x(z) = \frac{H_T \sinh{(\Psi z)} + H_B \sinh{(\Psi(h-z))}}{\sinh{(\Psi h)}}. \quad (19)$$

Using Ampere's law, $J_y(z) = \nabla \times H_x(z)$, the current density distribution in the conductor, $J_y(z)$, is

$$J_y(z) = \Psi \left[\frac{H_T e^{\Psi h} - H_B}{e^{\Psi h} - e^{-\Psi h}} e^{-\Psi(h-z)} - \frac{H_B e^{\Psi h} - H_T}{e^{\Psi h} - e^{-\Psi h}} e^{-\Psi z} \right]. \quad (20)$$

Finally, using Ohm's law, $J_y = \sigma E_y$, the electric field distribution inside the conductor, $E_y(z)$, is

$$E_y(z) = \frac{\Psi}{\sigma} \left[\frac{H_T e^{\Psi h} - H_B}{e^{\Psi h} - e^{-\Psi h}} e^{-\Psi(h-z)} - \frac{H_B e^{\Psi h} - H_T}{e^{\Psi h} - e^{-\Psi h}} e^{-\Psi z} \right]. \quad (21)$$

Hence, the field distribution and the current densities in the magnetic structure, within and outside the conductors, can be rapidly determined and visualized.

C. Parameter Extraction by Simulation

Numerous ways of modeling magnetic devices with one or more windings have been developed [24], [25], [33], [36]–[41]. Figure 10a shows the widely used cantilever model for magnetic structures with multiple windings [24]. This model is closely related to the inductance matrix description, which comprises self and mutual inductances of the multiple windings. Parameters in this inductance-based cantilever model can be experimentally found by conducting open- and short-circuit measurements. However, the accuracy of experimental measurements are limited by practical constraints (e.g. instrument capability). Moreover, as the frequency increases, the self and mutual resistances have a significant impact on current distribution, thus needs to be accurately modeled.

The proposed lumped circuit model integrally-captures the self and mutual inductances and resistances (i.e. impedances), enabling the development of an impedance-based cantilever model, as an enhancement to the inductance-based cantilever model. Figure 10b shows the proposed impedance-based cantilever model for an N winding structure. A resistance element is added in series with each inductance element to model the self and mutual resistances. For example, R_{11} and L_{11} model the self resistance and self inductance of winding W_1; and L_{jk} and R_{jk} (connects windings W_j and W_k) model the mutual resistance and mutual inductance between winding W_j and W_k (referred as mutual impedance $Z_{jk} = R_{jk} + j\omega L_{jk}$). The effective turns ratios, n_2 to n_N, represent the ratios of the voltages of winding W_2 to W_N to the voltage of winding W_1 under open-circuit conditions. With the presence of impedance elements in the model, the effective turns ratios, n_2 to n_N, are no longer real, but instead complex.
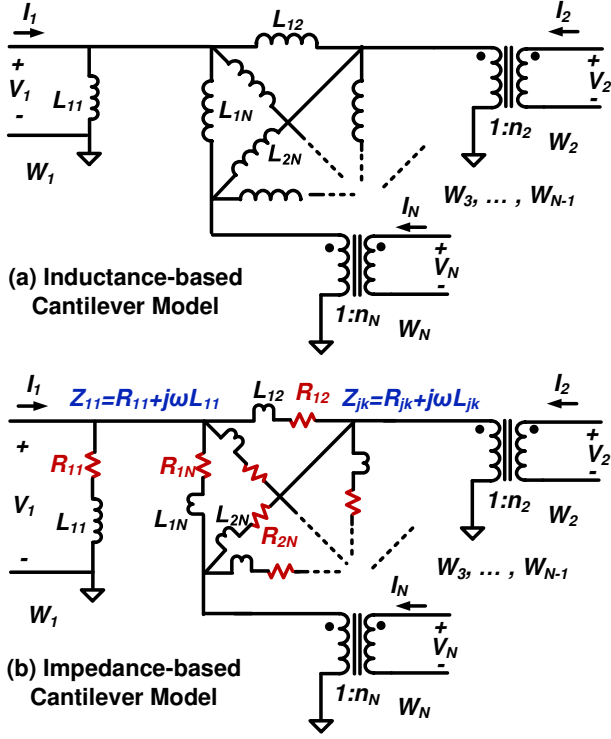
Fig. 10. (a) Conventional inductance-based cantilever model [24], and (b) proposed impedance-based cantilever model with self and mutual impedances.
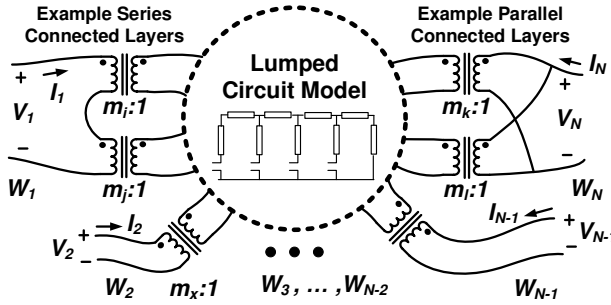

Fig. 11. Lumped circuit model that can be used to extract parameters for the impedance-based cantilever model, the impedance matrix, and the admittance matrix. Their perameters can be determined by open- and short-circuit simulations.

With the lumped circuit model, parameters of the impedance-based cantilever model can be extracted from circuit simulations, which are usually easier to implement and much faster than experimental measurements or FEM simulations. As shown in Fig. 11, the lumped circuit model uses N winding ports to represent the N physical ports of a magnetic device. All layer connections, electrical vias, field couplings, etc., are modeled and encapsulated behind the N ports. Each winding port in the lumped circuit model can be treated like a physical port in open- and short-circuit simulations. As a result, the parameter extraction method described in [24] (based on open and short circuit measurements) can be directly applied to the lumped circuit model.

These parameter extractions can be conducted by applying small-signal ac analysis in circuit simulations. The self impedance Z_{11} is determined by open-circuiting windings W_2 to W_N, and measuring the voltage and current of winding W_1. To measure the effective turns ratios n_2 to n_N, a voltage is applied to winding W_1. The open-circuit voltage of winding W_2-W_N are measured and recorded as v_1 to v_N. The effective turns ratio n_k is given by

$$n_k = \frac{v_k}{v_1}, k = 2, ..., N. \tag{22}$$

Note that n_k is complex as v_k and v_1 are both complex (n_k may have negative real and/or imaginary parts).

To measure the mutual impedance Z_{jk}, winding W_j is driven with a voltage source v_j, with all other windings short-circuited, and the current i_k in winding W_k is measured. The effective mutual impedance Z_{jk} is given by

$$Z_{jk} = \frac{v_j}{n_j n_k i_k}. \tag{23}$$

To normalize the model, n_1 is taken as 1. It is possible for Z_{jk} to have negative real and/or imaginary parts. Similar open- and short-circuit simulations can also be conducted to extract elements of the impedance matrix and the admittance matrix using the lumped circuit model [38], [39].

The impedance matrix $\{z_{jk}\}_{N \times N}$, admittance matrix $\{y_{jk}\}_{N \times N}$, the winding voltage vector $V_{N \times 1} = [v_1; ...; v_N]_{N \times 1}$, and the winding current vector $I_{N \times 1} = [i_1; ...; i_N]_{N \times 1}$ are related by

$$\begin{cases} V_{N \times 1} = \{z_{jk}\}_{N \times N} I_{N \times 1} \\ \{y_{jk}\}_{N \times N} V_{N \times 1} = I_{N \times 1} \\ \{z_{jk}\}_{N \times N} = \{y_{jk}\}_{N \times N}^{-1}. \end{cases} \tag{24}$$

The impedance-based cantilever model is closely related to the impedance matrix and the admittance matrix. Using Eq. 22 and Eq. 23 and corresponding measurement setups, the parameters of the impedance-based cantilever model can be found from $\{z_{jk}\}_{N \times N}$ and $\{y_{jk}\}_{N \times N}$ using

$$\begin{cases} Z_{11} = z_{11} \\ n_j = \frac{z_{1j}}{z_{11}} \\ Z_{jk} = -\frac{1}{n_j n_k y_{jk}}. \end{cases} \tag{25}$$

Conversely, the elements of $\{z_{jk}\}_{N \times N}$ and $\{y_{jk}\}_{N \times N}$ can be expressed in terms of the parameters of the impedance-based cantilever model by

$$\begin{cases} y_{jk} = -\frac{1}{n_j n_k Z_{jk}}, \text{when j} \neq \text{k} \\ y_{jj} = \frac{1}{n_j} \sum_{k=1}^{N} \frac{1}{z_{kj}}, \text{with z}_{jj} = \begin{cases} \infty \text{ if j} \neq 1 \\ Z_{11} \text{ when j} = 1 \end{cases} \\ \{z_{jk}\}_{N \times N} = \{y_{jk}\}_{N \times N}^{-1}. \end{cases} \tag{26}$$

Hence, the impedance-based cantilever model is interchangeable with the impedance matrix and the admittance matrix. As demonstrated, all parameters of the cantilever model, the impedance matrix, and the admittance matrix can be extracted from the lumped circuit model by rapid simulations.
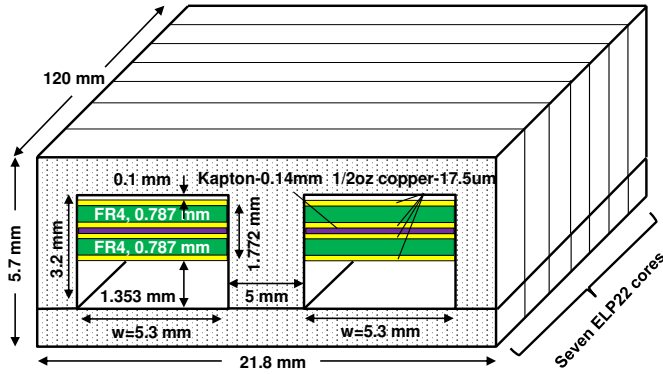
Fig. 12. Geometry of the seven-core four-layer structure. It is used to fabricate the 1:1 and 2:1 transformers. The calculated dc resistance of a single layer at $20°$C is 44.8mΩ, which is high enough to be measured with Agilent 4395A.
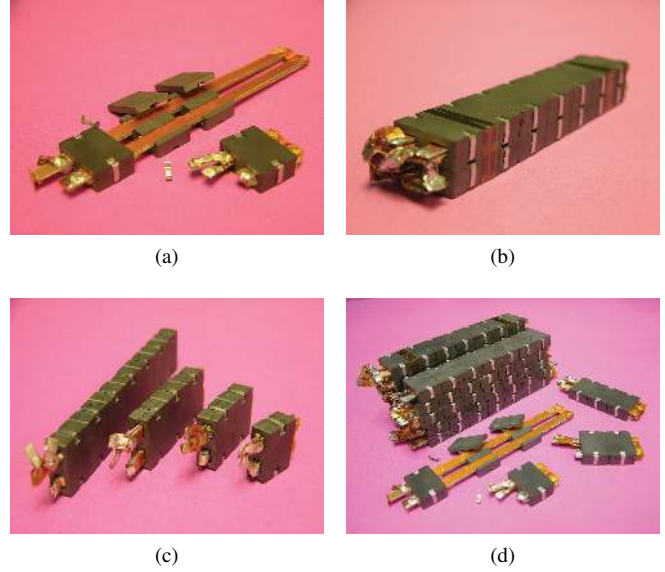

Fig. 13. Photographs of the constructed prototype: (a) copper layers and magnetic cores of a prototype. (b) Two 2:1 transformers connected and measured in the setup shown in Fig. 15b, (c) Four 1:1 transformers with different lengths (i.e. one core, two cores, three cores and seven cores), and (d) all constructed prototypes.

V. MODEL VERIFICATION AND APPLICATION EXAMPLES

As part of model verification, the model has been checked against prior known results, including expected values at dc, energy storage predictions based on the Poynting's theorem, and Dowell's results for series-connected multilayer windings [8]. These theoretical checks are presented in Appendix II.

To further verify the model, we compare the modeling results against FEM simulations and experimental measurements. These verifications also serve as application examples to demonstrate how to use the model in practical designs. Figure 12 shows the geometry of a selected example structure. It has four one-turn 17 μm thickness (half oz) copper layers, fabricated using two 0.787 mm (31 mil) thickness double-sided copper boards. A 0.14 mm thickness polyimide (Kapton) film was used as the spacing insulator between the two copper boards. Seven ELP22 cores of MnZn ferrite (Epcos N49) were lined up to make a long structure with impedances that were high enough to be accurately measured. Under this setup, since the permeability of the core was very high, the "1-D assumption" was satisfied. Cases with fewer cores and shorter length were were checked. The frequency range for testing was 10 kHz to 100 MHz. The operating temperature was selected to be $20°$C. Figure 13 shows a few pictures of these prototypes. For each group of devices, interleaving patterns can have significant impact on the impedances and current distributions, as does the spacing of the PCB layer stacks. Three types of magnetic devices, which represent a majority of possible interleaving patterns, are prototyped by connecting the four copper layers in three ways:

1) **1:1 transformers with parallel-connected layers**: two layers are connected in parallel as a one-turn winding; two layers are connected in parallel as another one-turn winding.

2) **2:1 transformers with hybrid series-parallel-connected layers**: two layers are connected in series as a two-turn winding; two layers are connected in parallel as a one-turn winding.

3) **One-turn inductors with parallel-connected layers**:

two layers are selected and connected in parallel as a one-turn winding; the other two layers are not used (manufactured using two single-sided copper boards).

The goal is to compare the predicted and measured ac resistance (R_{ac}) and ac inductance (L_{ac}) in these structures under the setup as shown in Fig. 15 when they are operating in the 10 kHz to 100 MHz frequency range. This verification strategy is similar to the setup used in [42].

A. 1:1 transformers with parallel-connected layers

Figure 14 shows three different ways of connecting the four layers in a 1:1 transformer having two paralleled layers in each winding, including one non-interleaved option and two interleaved options. The measurement setup is shown in Fig. 15a. This setup avoids exciting the magnetizing flux path in the core, and thus reduces the impact of core losses on the verification results. Figure 16 shows the lumped circuit model for the four layer structure. Note that in this setup, the impedances associated with the top and bottom magnetic cores (Z_{ts}, Z_{tf}, Z_{bs}, Z_{bf} in Fig. 7) carry no flux. Considering cross-layer connections (electrical vias), three simplified circuits shown in Fig. 17 can be generated. One can easily analyze these circuits, and compare the R_{ac} and L_{ac} in each case.

In addition, FEM models for these structures are analyzed using ANSYS Maxwell FEM simulation package. Figure 18 shows the magnetic field strength in the three structures when they are operating at 10 MHz. The dissipated power (P_{ac}) and stored reactive energy (E_{ac}) in these structures as a function of frequency are found by the software, leading to the simulated R_{ac} and L_{ac} determined by FEM methods. Finally, the ac resistance (R_{ac}) and ac inductance (L_{ac}) of these
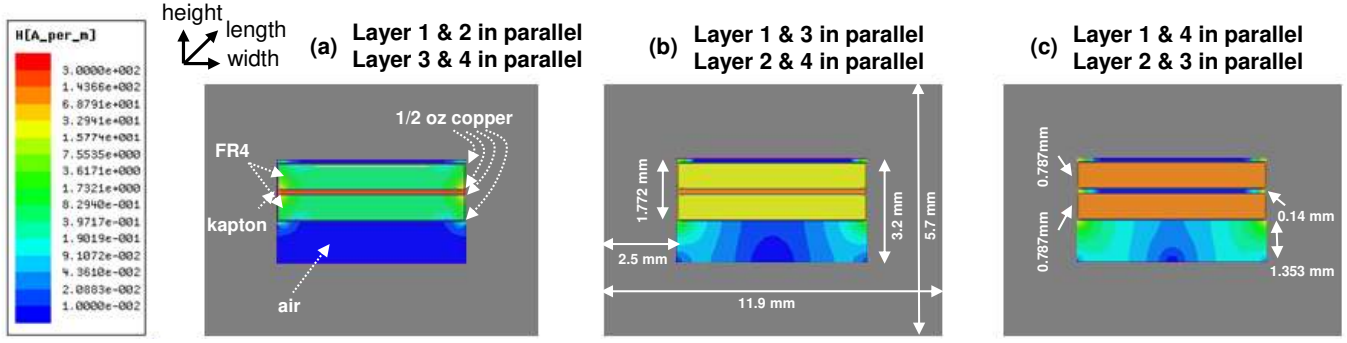
Fig. 18. Magnetic field distribution in three 1:1 transformers having two paralleled layers for each winding, each with different interleaving patterns, driven by a 10 MHz 1 A (peak) current (under the setup as shown in Fig. 15a). Layer indices from top to bottom are: layer 1, layer 2, layer 3, layer 4. The simulation was done in 2-D with the transformer length infinitely long.
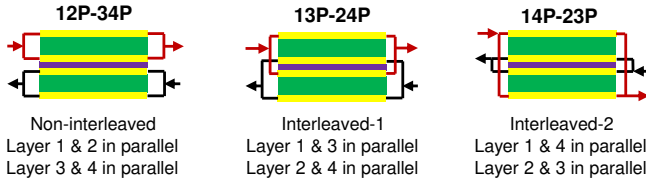

Fig. 14. Three different ways of interleaving the four conductor layers in a 1:1 transformer having two paralleled layers for each winding, including a non-interleaved option and two interleaved options.

Fig. 15. Experimental configurations for measuring (a) 1:1 transformers with two-parallel-layer pairs; (b) 2:1 transformers with hybrid-series-parallel windings pairs. These configurations avoid exciting the core and thus greatly reduce the impact of core losses on the results. Core loss is not captured in this lumped circuit model. If one would like to include the modeling of core loss, it could be represented as a resistance R_M in parallel with L_M.

Fig. 16. Lumped circuit model for the structure shown in Fig. 12 without modeling the electrical vias.
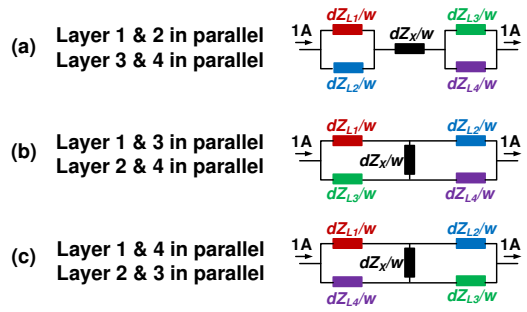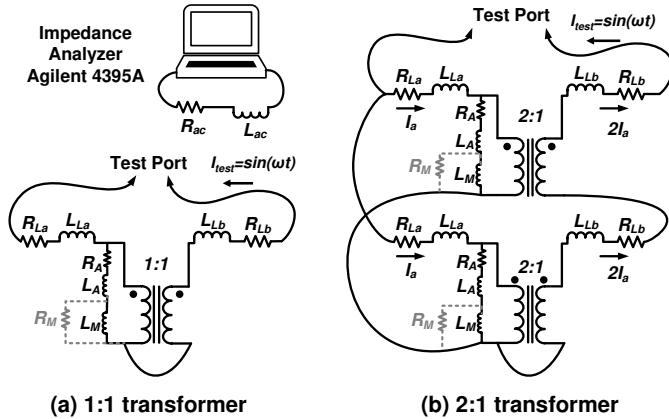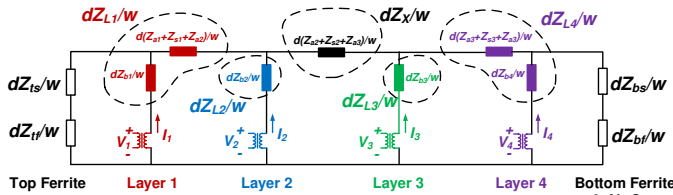

Fig. 17. Lumped circuit model for the three interleaving patterns of the 1:1 transformer, including the vias. Since the core is not excited, the impedances representing the core in Fig. 16 have been removed from this figure.

transformers are measured using an Agilent 4395A impedance analyzer under the setup of Fig. 15a. As shown in Fig. 19, the results from the lumped circuit model match extremely well with FEM simulations over the entire frequency range, and match well with experimental measurements. A few practical constraints that may cause mismatches are investigated in Section VI.

Conventionally, it is qualitatively known that as the operating frequency increases, skin and proximity effects change the current distribution, changing the real and reactive impedances of a magnetic device. The proposed approach is a powerful tool to quantitatively study these complicated frequency dependent effects. Many qualitative and quantitative findings can be observed from Fig. 19; among those are:

1) Starting from 100 kHz, interleaved connections ("13P-24P" and "14P-23P") have lower loss than the non-interleaved connection ("12P-34P"). The loss reduction can be as high as 50% at 10 MHz.

2) Between the two interleaved structures, the loss of "14P-23P" can be up to 37.5% lower than that of "13P-24P" at 10 MHz. This is because the current directions in layers 2 and 3 are opposite to each other in "13P-24P", with narrow spacing in between (Polyimide film). As a result, a big portion of current concentrates in layer 2 and 3, causing high loss. This may alternatively be viewed as
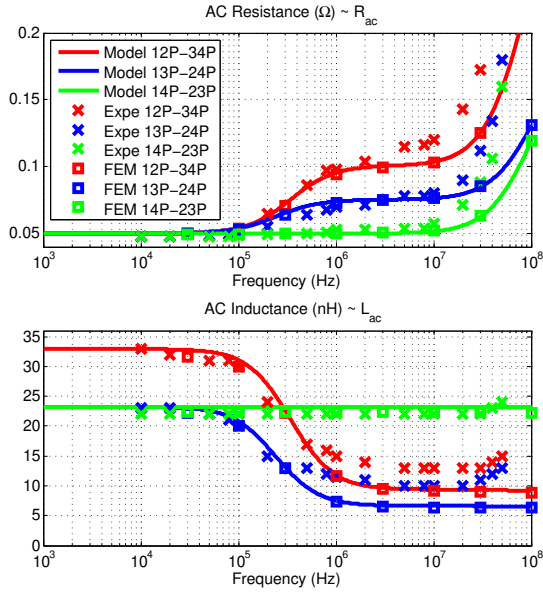
Fig. 19. R_{ac} and L_{ac} of the planar structure predicted by the proposed approach (Model), simulated by ANSYS (FEM), and measured from the prototype (Expe). Note: "12P-34P" indicates that layer 1 and layer 2 are connected in parallel as one winding, and layer 3 and layer 4 are connected in parallel as the other winding.

the "13P-24P" having more circulating current in the parallel layers and hence higher loss. As the proposed model well predicts this effect, the model is well suited to selecting interleaving configurations (especially when there are parallel layers) to minimize loss.

3) Whether "14P-23P" or "13P-24P" has higher ac resistance actually depends on the PCB layer stack spacings. Figure 20 shows two selected layer stacks for comparison purposes. One layer stack has thin Polyimide film (0.14 mm) as the middle spacing (Polyimide-Mid). This layer stack is also the default layer stack used in this paper. The other layer stack, in comparison, employs a thick FR4 board (1.574 mm) as the middle spacing (FR4-Mid). The winding width, length, height, core shape and other experimental aspects are the kept the same as described in Fig. 12. The R_{ac} and L_{ac} in the two PCB layer stacks with different interleaving patterns are shown in Fig. 21. With the "Polyimide-Mid" layer stack, "14P-23P" has significantly lower R_{ac} than "13P-24P". With the "FR4-Mid" layer stack, however, "14P-23P" has slightly higher R_{ac} than "13P-24P". This example demonstrates that the proposed approach can be used to select the optimal interleaving structure that has the minimum R_{ac} for a chosen PCB layer stack spacing, and/or to optimally select PCB stack spacings.

The change of the ac resistance is caused by the redistribution of current and magnetic field, which also changes the reactive impedance of the planar structure (e.g. leakage inductances of transformers). The proposed approach can be used to select the optimal interleav-
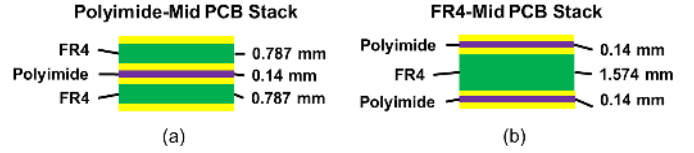

Fig. 20. Two PCB layer stacks having different spacings between layers: (a) Polyimide-Mid: with polyimide film as the middle spacing; (b) FR4-Mid: with FR4 board as the middle spacing.
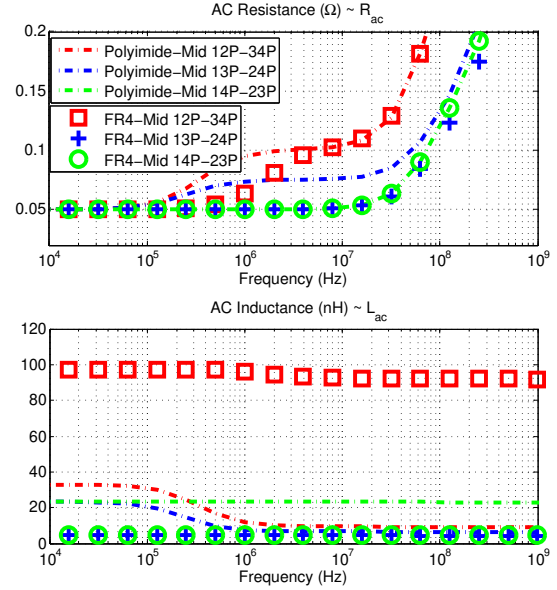

Fig. 21. R_{ac} and L_{ac} of the 1:1 transformer for two different PCB layer stacks. One layer stack has Polyimide film as the middle spacing (Polyimide-Mid). The other layer stack has FR4 board as the middle spacing (FR4-Mid).

ing structure that has the most appropriate reactive impedance. As shown in Fig. 21, for the "Polyimide-Mid" layer stack, "12P-34P" has high L_{ac} at low frequencies because it excites high magnetic fields in both the FR4 spacings and the Polyimide spacing. The L_{ac} of "12P-34P" and "13P-24P" drop as the frequency increases, because as current concentrates in the middle layers, energy stored in the spacings and within conductors decreases. Considering various interleaving patterns and PCB layer stacks, the proposed approach can be used to accurately model the reactive impedance in a magnetic device, enabling multiple correlated design tradeoffs to be made integrally (e.g. when designing an efficient transformer for a LLC converter).

B. 2:1 transformers with hybrid-series-parallel layers

The purpose of this experiment is to verify the effectiveness of the proposed approach for modeling planar magnetics with hybrid series- and parallel-connected layers. Figure 22 shows three different ways one may connect the four layers to construct a 2:1 transformer with both series- and parallel-connected layers. Two layers are series-connected as a two-turn primary winding, and two layers are parallel-connected as a one-turn secondary winding. Because the primary current
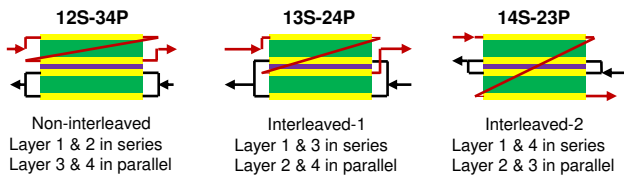
Fig. 22. Three different interleaving patterns of the hybrid-series-parallel 2:1 transformer having a winding comprising two series-connected layers and a winding comprising two parallel-connected layers.
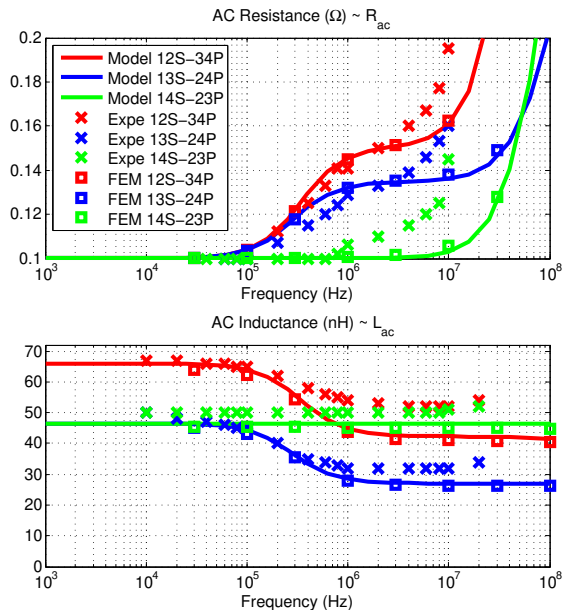

Fig. 23. R_{ac} and L_{ac} of the planar transformer with 2:1 hybrid series-parallel layers predicted by the lumped model (Model), simulated by ANSYS (FEM), and measured from the prototype (Expe).

is twice as large as the secondary current, a "parallel-primary series-secondary" setup as shown in Fig. 15b is utilized to measure winding impedances while avoiding exciting the magnetizing inductance. This setup needs two identical 2:1 transformers. Figure 23 compares the modeling results, FEM results and measurement results. The lumped model results match very well with FEM simulations over the entire frequency range, and match experimental results within 20% up to 10 MHz. This setup has higher mismatch than the 1:1 transformer setup because the two transformers connected to make the measurement are not entirely identical (i.e. exciting the core to the same extend), and the interconnects between the two transformers are not captured in the model. Nevertheless, the results demonstrate the efficacy of the proposed approach for capturing the behavior of sophisticated winding structures.

C. One-turn inductors with parallel-connected layers

The purpose of this experiment is to verify the effectiveness of the proposed approach for modeling planar magnetics with excited cores (e.g. inductors) and parallel-connected layers. The modeling results for inductors with series-connected layers are theoretically verified by comparing them with Dowell's
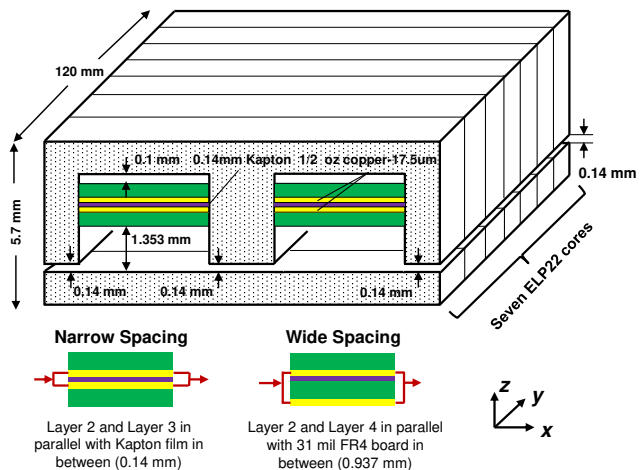

Fig. 24. Geometries of the prototyped two-parallel-layer inductors. Two layers out of the four layers are selected and connected in parallel. One implementation has a narrow spacing between the two parallel-connected layers. The other implementation has a wide spacing between the two parallel-connected layers.

formulation (Appendix II). Figure 24 shows the geometry and layer connections of an inductor with two parallel-connected layers. In one inductor, layers 2 and 3 are selected and paralleled. This inductor has narrow spacing between two layers (polyimide film). In the other inductor, layers 2 and 4 are selected and paralleled. This inductor has wide spacing between two layers (FR4 broad and polyimide film). The ac resistance and ac inductance of this inductor are measured with an impedance analyzer (100 kHz-1 MHz). The core loss can be estimated by using the datasheet, and subtracted to yield the winding loss. At the same time, the R_{ac} and L_{ac} are predicted using the proposed model and FEM simulations. As shown in Fig. 25, the results from the model match very well with FEM results, and match well with experimental results up to 1 MHz (This is the highest recommended operating frequency for the EPCOS N49 MnZn material with known core loss). No effort has been made to measure its core loss above 1 MHz. Optimally designed low loss litz wire [43] with accurate winding loss estimation may be used to better calibrate/verify the core loss.

VI. PRACTICAL CONSTRAINTS AND CONSIDERATIONS

The proposed modeling approach is developed based on the "MQS assumption" and the "1-D assumption". In most power electronics applications, the operating frequency is low enough for the "MQS assumption" to hold. However, many practical designs may not satisfy the "1-D assumption" well, causing mismatches between model predictions and measured results. Here we discuss some of these cases along with ways to address them.

1) **End effects**: As shown in Fig. 26a, in some core shapes, e.g., ELP cores, a portion of the conductor is not covered by the magnetic core. They no longer satisfy the "1-D assumption". To investigate this, we experimentally measured the R_{ac} and L_{ac} in four 1:1 transformers

(a) Mismatch as a function of the "e/(2l+e)" ratio for end effects.

(b) Mismatch as a function of the "c/w_w" ratio for side spacing.

(c) Mismatch as a function of the "c/w_w" ratio for middle spacing.
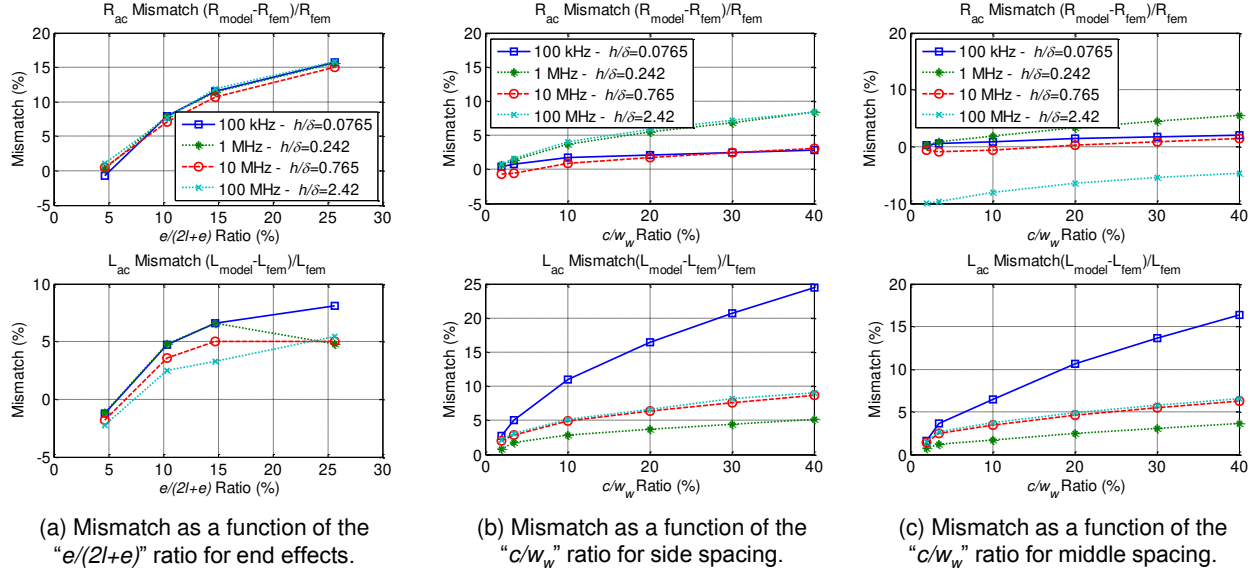
Fig. 27. Mismatch between the modeling results and FEM results when considering (a) end effects, (b) conductor-core clearances, and (c) conductor-conductor clearances. Mismatch is defined as the ratio of the difference between modeling and FEM results. Here h is the thickness of the copper layer (h is default to be half oz, 17.5 μm, in this paper), and δ is the skin depth of the conductor depending on the operating frequency.
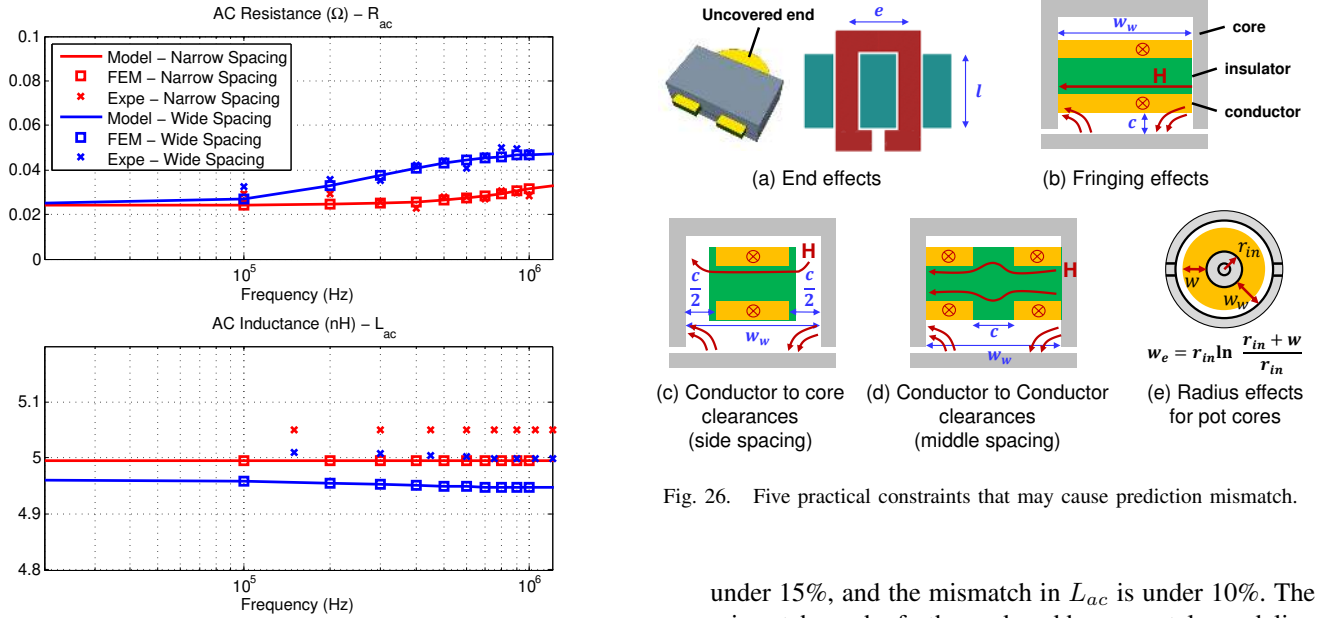

Fig. 25. Comparison of R_{ac} and L_{ac} results for two prototypes based on the lumped circuit model (Model), FEM simulations (FEM) and experimental measurements (Expe).

(a) End effects
(b) Fringing effects

(c) Conductor to core clearances (side spacing)
(d) Conductor to Conductor clearances (middle spacing)
(e) Radius effects for pot cores

$$w_e = r_{in}\ln \frac{r_{in}+w}{r_{in}}$$

Fig. 26. Five practical constraints that may cause prediction mismatch.

with different numbers of cores (as shown in Fig. 13c). The mismatch as a function of the "end-to-length" ratio ($e/(2l+e)$) and the "conductor-thickness to skin-depth" ratio (h/δ) are presented in Fig. 27a. The mismatch due to end effects does not have a strong dependence on frequency (i.e. h/δ ratio) but is a strong function of the $e/(2l+e)$ ratio. However, in this specific setup, as long as $e/(2l+e)$ is smaller than 25%, the mismatch in R_{ac} is

under 15%, and the mismatch in L_{ac} is under 10%. The mismatch can be further reduced by separately modeling and calibrating the impedances of the uncovered ends.

2) **Fringing effects**: As shown in Fig. 26b, if conductor layers are placed near the air gap, fringing fields can penetrate the windings and change the current distribution, causing modeling mismatches (usually leading to underestimated conduction losses). This effect has been numerically analyzed in [13], [44], and it was recommended in [44] that the clearance (c) be at least 25% of the total window width w_w (i.e. gap to gap spacing) to limit the fringing effects.

3) **Conductor-core clearances (side spacing)**: As shown in Fig. 26c, clearances are required between conductors and PCB edges, and between PCB edges and the core.

These clearances change the dissipated loss and stored reactive energy. Figure 27b shows the mismatch between the model prediction and FEM results as a function of the "clearance to window-width" ratio (c/w_w), and the "conductor-thickness to skin-depth" ratio (h/δ) for the 1:1 transformers described in Section V-A. Up to frequencies where h/δ equals 2.42 (100 MHz for half-oz copper), the mismatch of the R_{ac} is less than 10% if c/w_w is smaller than 40%. For accurate estimation of L_{ac}, it is preferable if h/δ is smaller than 1. Note, for half-oz copper (17.5 μm), the frequency when h/δ equals 1 is approximately 14 MHz.

4) **Conductor-conductor clearances (middle spacing)**: As shown in Fig. 26d, clearances between two adjacent turns can also cause mismatches. Figure 27c shows the increase in mismatch as the c/w_w ratio increases. Up to frequencies when h/δ equals 2.42, the mismatch in R_{ac} is less than 10% if c/w_w is smaller than 40%. To achieve accurate estimation for L_{ac}, it is preferable if the h/δ ratio is below 1.

5) **Radius effects for pot cores**: Figure 26e shows a pot core whose window width (w_w) is comparable to its window inner radius (r_{in}). In this situation, the magnetic field and current distributions along the radius follows a "logarithmic" distribution similar to that described in [10]. Assuming that the conductive layer fills the window width (i.e. $w = w_w$), this effect can be included in the lumped circuit model by replacing the layer width (w) in the impedance calculations with an effective width $w_e = r_{\mathrm{in}} \ln(1 + \frac{w}{r_{\mathrm{in}}})$ (Note: $\lim_{r_{\mathrm{in}} \to +\infty} w_e = w$).

VII. Conclusions

This paper presents a systematic approach to modeling impedances and current distribution in planar magnetics. The electromagnetic interactions in planar magnetics are clarified, organized and converted into a lumped circuit model under the "1-D" and "MQS" assumptions. The lumped circuit model can be used to estimate the ac impedances, to determine current sharing in parallel windings, and to extract parameters for an impedance-based cantilever model, among many other magnetic models. The proposed approach is verified by existing theories, FEM simulations, and experimental measurements. The modeling performance under a few practical constraints is investigated and discussed to clarify the boundaries of applicability. It is demonstrated that the approach performs very well in modeling commonly used planar magnetics.

Acknowledgment

Appendix I: Derivation of the Lumped Circuit Model

This appendix derives the lumped circuit model in detail. All variables are the same as those utilized in Section II.

A. Modeling a one-turn layer

Under the "1-D" approximation, the magnetic field within a conductive layer satisfies the 1-D diffusion equation [37]

$$\frac{1}{\mu\sigma}\nabla^2 H_x = \frac{dH_x}{dt}. \tag{27}$$

Its solution is

$$H_x(z) = \frac{[H_T \sinh(\Psi z) + H_B \sinh(\Psi(h - z))]}{\sinh(\Psi h)}. \tag{28}$$

Here $\Psi = \frac{1+j}{\delta}$, $\delta = \sqrt{\frac{2}{\mu_r\mu_0\omega\sigma}}$. Using Ampere's Law under the MQS approximation: $\nabla \times H_x(z) = J_y(z) = \sigma E_y(z)$, gives

$$E_y(z) = \frac{\Psi}{\sigma}\left[\frac{H_T e^{\Psi h} - H_B}{e^{\Psi h} - e^{-\Psi h}}e^{-\Psi(h-z)} - \frac{H_B e^{\Psi h} - H_T}{e^{\Psi h} - e^{-\Psi h}}e^{-\Psi z}\right]. \tag{29}$$

At the top and bottom surface of the conductor (i.e. when $z = 0$ and $z = h$), (29) gives

$$\begin{aligned} E_T = E_y(h) &= \frac{\Psi}{\sigma}\left[\frac{H_T e^{\Psi h} - H_B}{e^{\Psi h} - e^{-\Psi h}} - \frac{H_B - H_T e^{-\Psi h}}{e^{\Psi h} - e^{-\Psi h}}\right] \\ E_B = E_y(0) &= \frac{\Psi}{\sigma}\left[\frac{H_T - H_B e^{-\Psi h}}{e^{\Psi h} - e^{-\Psi h}} - \frac{H_B e^{\Psi h} - H_T}{e^{\Psi h} - e^{-\Psi h}}\right]. \end{aligned} \tag{30}$$

Defining impedance Z_a and Z_b as

$$\begin{aligned} Z_a &= \frac{\Psi(1 - e^{-\Psi h})}{\sigma(1 + e^{-\Psi h})} \\ Z_b &= \frac{2\Psi e^{-\Psi h}}{\sigma(1 - e^{-2\Psi h})}, \end{aligned} \tag{31}$$

allows (30) to be simplified to

$$\begin{aligned} E_T &= Z_a H_T + Z_b(H_T - H_B) \\ E_B &= Z_b(H_T - H_B) - Z_a H_B. \end{aligned} \tag{32}$$

Also by Ampere's Law

$$(H_T - H_B)w = I = Kw, \tag{33}$$

combining (32) and (33), we get

$$\begin{aligned} E_T &= Z_a H_T + Z_b K \\ E_B &= Z_b K - Z_a H_B. \end{aligned} \tag{34}$$

This yields (1) in Section II.

B. Modeling two adjacent one-turn layers

In Fig. 4, consider a closed loop surrounding the center post that includes the bottom surface of layer 1 and the external voltage source V_1. Applying Faraday's law to the loop gives

$$E_{B1}d - V_1 = -\frac{d\Phi_{B1}}{dt}, \tag{35}$$

where Φ_{B1} is the magnetic flux in the center post across the bottom surface of layer 1. Similarly, consider a closed loop surrounding the center post that includes the top surface of layer 2 and the external voltage source V_2,
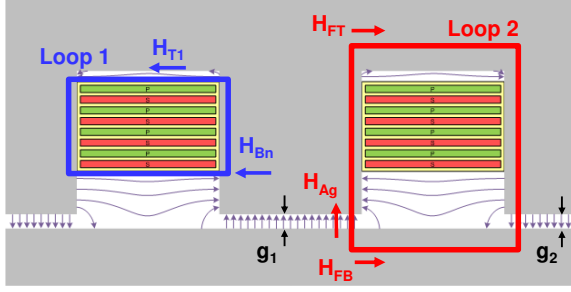
$$E_{T2}d - V_2 = -\frac{d\Phi_{T2}}{dt}, \tag{36}$$

Fig. 28. Two H field loops for deriving the impedances representing the core and the air gap.

where Φ_{T2} is the magnetic flux in the center post across the top surface of layer 2. Now, the magnetic flux penetrating into the center post through the spacing between the two layers (Φ_{S12}), equals $\mu_0 a_1 dH_{S12}$. Using flux continuity, $\Phi_{T2} = \Phi_{B1} + \Phi_{S12}$, and taking the derivative gives

$$\frac{d\Phi_{T2}}{dt} = \frac{d\Phi_{B1}}{dt} + \frac{d\Phi_{S12}}{dt}. \tag{37}$$

Combining (35)-(37) gives

$$H_{S12} = \frac{1}{j\omega\mu_0 a_1}\left(\frac{V_2}{d} - E_{T2} - \frac{V_1}{d} + E_{B1}\right). \tag{38}$$

This yields (6) in Section II.

C. Modeling the magnetic core and the air gap

Loop 1 in Fig. 28 comprises the spacing between the top surface of layer 1 and the core, the center post, the spacing between bottom surface of layer n and the core, and the outer surface. Integrating the magnetic field in this loop gives

$$(H_{T1} - H_{Bn})w = \sum_{i=1}^{n} I_i. \tag{39}$$

Here we only include the top and bottom sides of the loop, because either the high permeability of the core makes the H value inside of it negligible, or the length of the core legs is much smaller than the window width. Loop 2 in Fig. 28 comprises the top of the core, the center post, the air gap and the bottom of the core. Integrating the magnetic field along this loop gives

$$H_{Ag}(g_1 + g_2) - H_{FB}w + H_{FT}w = \sum_{i=1}^{n} I_i. \tag{40}$$

Here H_{Ag} is the field strength in the air gap, H_{FT} is the field strength in the top magnetic core, H_{FB} is the field strength in the bottom magnetic core, and $(g_1 + g_2)$ is the total length of the air gap. Using flux continuity,

$$\begin{aligned} H_{T1} &= H_{FT} \\ \mu_0\mu_r c_b dH_{FB} &= -\mu_0 A_c H_{Ag}. \end{aligned} \tag{41}$$

Combining (39)-(41), H_{Ag} can be calculated from H_{Bn}

$$H_{Ag} = -\frac{H_{Bn}w}{g_1 + g_2 + \frac{A_c w}{\mu_r c d}}. \tag{42}$$

The magnetic flux that flows through the center post and across the top surface of layer 1, Φ_{T1}, is

$$\Phi_{T1} = \mu_r\mu_0 cdH_{FT} + \mu_0 b_t dH_{T1} = (\mu_r\mu_0 cd + \mu_0 b_t d)H_{T1}. \tag{43}$$

Using Faraday's law and integrating the electric field along the top surface of layer 1 and the external voltage source V_1

$$E_{T1} - \frac{V_1}{d} = -j\omega\mu_r\mu_0 c_b H_{T1} - j\omega\mu_0 b_t H_{T1}. \tag{44}$$

Similarly, the magnetic flux flowing through the center post and across the bottom surface of layer n, Φ_{Bn}, is

$$\Phi_{Bn} = \mu_0 A_c H_{Ag} - \mu_0 bdH_{T1} = -\frac{\mu_0 A_c w}{g + \frac{A_c w}{\mu_r c_b d}}H_{Bn} - \mu_0 b_b dH_{Bn}. \tag{45}$$

Integrating the electric field along the bottom surface of layer n, and the external voltage source V_n, gives

$$E_{Bn} - \frac{V_n}{d} = j\omega\frac{\mu_0 A_c w}{g + \frac{A_c w}{\mu_r c_b d}}H_{Bn} + j\omega\mu_0 b_b H_{Bn}. \tag{46}$$

Hence, (9) and (10) in section II are derived.

APPENDIX II: THEORETICAL VERIFICATIONS

The proposed modeling approach can be theoretically verified by checking its results against some known results.

A. Current distribution at dc

The proposed modeling approach can be checked to ensure that it predicts correct results in the extreme case when the conductor carries dc current ($\omega \to 0$). For the one-turn layer shown in Fig. 3, if $\omega \to 0$, then $\delta \to \infty$, and $\Psi \to 0$. Using (21), the current distribution at dc is

$$\lim_{\Psi \to 0} J_y(z) = \lim_{\Psi \to 0}\frac{2(H_T - H_B)\Psi}{e^{\Psi h} - e^{-\Psi h}} = \frac{K}{h}. \tag{47}$$

This indicates that the current distribution is a constant along the conductor thickness when $\omega \to 0$, which is as expected.

B. Poynting's theorem and energy conservation

The energy processed in any structure must satisfy the Poynting's theorem: the power dissipated and stored within it must equal the integral of the Poynting vector over a closed surface boundary cutting into this surface. In Fig. 5a, assuming that there is no spacing between two series-connected turns on the same layer, and that all turns have the same width $\frac{w}{m_1}$, the complex power dissipated and stored in layer 1 is

$$P_{poynting} = \underbrace{dw}_{\text{Surface Area}}\underbrace{(E_{T1}H_{T1}^* - E_{B1}H_{B1}^*)}_{\text{Poynting vectors}}. \tag{48}$$

Now consider the three-terminal impedance network of "Layer 1" in Fig. 5b. The electrical power going into layer 1 is

$$P_{model} = \underbrace{\frac{V_1}{m_1}m_1 I_1^* + (\frac{V_1}{m_1} - E_{B1}d)wH_{B1}^* - (\frac{V_1}{m_1} - E_{T1}d)wH_{T1}^*}_{\text{Electrical power of the three terminals}}$$

$$= dw(E_{T1}H_{T1}^* - E_{B1}H_{B1}^*). \tag{49}$$

Hence, the match between (48) and (49) shows that the proposed model predicts the same loss and energy storage in a layer as the Poynting's theorem. The energy conservation rule holds.

C. Dowell's formulation

For planar structures with multiple adjacent layers connected in series, the proposed approach can be used to derive the well-known Dowell's formulation [8]–[11]. Considering the planar structure shown in Fig. 6 and Fig. 7, if all n layers are one-turn layers with identical thicknesses h and width w, and all n layers are connected in series, the ac impedance of this n layer structure is

$$Z_{ac} = \left(nZ_b + 2Z_a \sum_{k=1}^{n-1} k^2 + n^2 Z_a \right). \tag{50}$$

Substituting (14) into (50), the ac resistance (R_{ac}) can be found as the real part of Z_{ac}:

$$R_{ac} = \Re(Z_{ac}) = R_{dc}\Delta \times \Re\left[\coth(\Delta(1+i))(1+i)\right] + R_{dc}\frac{2(n^2-1)}{3}\Delta \times \Re\left[\tanh(\frac{\Delta}{2}(1+i))(1+i)\right]. \tag{51}$$

Here R_{dc} is the dc resistance of the n series-connected layers

$$R_{dc} = \frac{nd}{\sigma wh}. \tag{52}$$

And Δ is the "thickness-to-skin-depth" ratio ($\frac{h}{\delta}$). Since

$$\Re\left[\coth(\Delta(1+i))(1+i)\right] = \frac{\sinh(2\Delta) + \sin(2\Delta)}{\cosh(2\Delta) - \cos(2\Delta)}$$
$$\Re\left[\tanh(\frac{\Delta}{2}(1+i))(1+i)\right] = \frac{\sinh(\Delta) - \sin(\Delta)}{\cosh(\Delta) + \cos(\Delta)}, \tag{53}$$

the ac resistance to dc resistance ratio, $F_R = \frac{R_{ac}}{R_{dc}}$, is

$$F_R = \Delta\left(\frac{\sinh(2\Delta) + \sin(2\Delta)}{\cosh(2\Delta) - \cos(2\Delta)} + \frac{2(n^2-1)}{3}\frac{\sinh(\Delta) - \sin(\Delta)}{\cosh(\Delta) + \cos(\Delta)}\right) \tag{54}$$

This is the well-known Dowell's formulation.

REFERENCES

[1] A.M. Urling, V.A. Niemela, G.R. Skutt and T.G. Wilson, "Characterizing high-frequency effects in transformer windings-a guide to several significant articles," *Proceedings of the IEEE Applied Power Electronics Conference and Exposition (APEC)*, pp. 373-385, 13-17 Mar. 1989.

[2] M.T. Quirke, J.J. Barrett, and M. Hayes, "Planar magnetic component technology-a review," *IEEE Transactions on Components, Hybrids, and Manufacturing Technology*, vol.15, no.5, pp. 884-892, Oct. 1992.

[3] N. Dai, A. W. Lofti, G. Skutt, W. Tabisz and F.C. Lee, "A comparative study of high-frequency, low-profile planar transformer technologies," *Proceedings of the IEEE Applied Power Electronics Conference and Exposition (APEC)*, pp. 226-232, vol.1, Feb. 1994.

[4] Z. Ouyang and M. Andersen, "Overview of planar magnetic technology - fundamental properties," *IEEE Transactions on Power Electronics*, vol. 29, no. 9, pp. 4888-4900, Sept. 2014.

[5] D.J. Perreault, J. Hu, J.M. Rivas, Y. Han, O. Leitermann, R.C.N. Pilawa-Podgurski, A. Sagneri, and C.R. Sullivan, "Opportunities and challenges in very high frequency power conversion," *Proceedings of the IEEE Applied Power Electronics Conference and Exposition (APEC)*, pp. 1-14, Feb. 2009.

[6] C.R. Sullivan, D.V. Harburg, J. Qiu, C.G. Levey, and D. Yao, "Integrating magnetics for on-chip power: a perspective," *IEEE Transactions on Power Electronics*, vol. 28, no. 9, pp. 4342-4353, Sept. 2013.

[7] M. Araghchini, J. Chen, V. Doan-Nguyen, D.V. Harburg, D. Jin, J. Kim, M.S. Kim, S. Lim, B. Lu, D. Piedra, J. Qiu, J. Ranson, M. Sun, X. Yu, H. Yun, M.G. Allen, J.A. del Alamo, G. DesGroseilliers, F. Herrault, J.H. Lang, C.G. Levey, C.B. Murray, D. Otten, T. Palacios, D.J. Perreault and C.R. Sullivan, "A technology overview of the PowerChip development program," *IEEE Transactions on Power Electronics*, vol. 28, no. 9, pp. 4182-4201, Sept. 2013.

[8] P.L. Dowell, "Effects of eddy currents in transformer windings," *Proceedings of the Institution of Electrical Engineers*, vol. 113, no. 8, pp. 1387-1394, Aug. 1966.

[9] J.H. Spreen, "Electrical terminal representation of conductor loss in transformers," *IEEE Transactions on Power Electronics*, vol. 5, no. 4, pp. 424-429, Oct. 1990.

[10] W.G. Hurley and M.C. Duffy, "Calculation of self and mutual impedances in planar magnetic structures," *IEEE Transactions on Magnetics*, vol. 31, no. 4, pp. 2416-2422, Jul. 1995.

[11] W.G. Hurley, E. Gath and J.G. Breslin, "Optimizing the AC resistance of multilayer transformer windings with arbitrary current waveforms," *IEEE Transactions on Power Electronics*, vol. 15, no. 2, pp. 369-376, Mar. 2000.

[12] C.R. Sullivan, "Computationally efficient winding loss calculation with multiple windings, arbitrary waveforms, and two-dimensional or three-dimensional field geometry," *IEEE Transactions on Power Electronics*, vol. 16, no. 1, pp. 142-150, Jan. 2001.

[13] A.F. Goldberg, J.G. Kassakian and M.F. Schlecht, "Issues related to 1-10-MHz transformer design," *IEEE Transactions on Power Electronics*, vol. 4, no. 1, pp. 113-123, Jan. 1989.

[14] A.F. Goldberg, J.G. Kassakian and M.F. Schlecht, "Finite-element analysis of copper loss in 1-10 MHz transformers," *IEEE Transactions on Power Electronics*, vol. 4, no. 2, pp. 157-167, Apr. 1989.

[15] A.F. Goldberg and M.F. Schlecht, "The relationship between size and dissipated power in a 1-10 MHz transformer," *IEEE Transactions on Power Electronics*, vol. 7, no. 1, pp. 63-74, Jan. 1992.

[16] C..P. Steinmetz, "On the law of hysteresis," *Proceedings of the IEEE*, vol. 72, no. 2, pp. 197-221, Feb. 1984.

[17] W.-J. Gu and R. Liu, "A study of volume and weight vs. frequency for high-frequency transformers," *Power Electronics Specialists Conference (PESC)*, pp. 1123-1129, 20-24 Jun. 1993.

[18] J. Li, T. Abdallah, and C.R. Sullivan, "Improved calculation of core loss with nonsinusoidal waveforms," *Proceedings of the Annual Meeting of IEEE Industry Applications Society*, pp. 2203-2210, vol. 4, Sept. 2001.

[19] K. Venkatachalam, C.R. Sullivan, T. Abdallah and H. Tacca, "Accurate prediction of ferrite core loss with nonsinusoidal waveforms using only Steinmetz parameters," *Proceedings of IEEE Workshop on Computers in Power Electronics (COMPEL)*, pp. 36-41, 3-4 Jun. 2002.

[20] J. Muhlethaler, J. Biela, J.W. Kolar and A. Ecklebe, "Core losses under the DC bias condition based on Steinmetz parameters," *IEEE Transactions on Power Electronics*, vol. 27, no. 2, pp. 953-963, Feb. 2012.

[21] Y. Han, G. Cheung, A. Li, C.R. Sullivan and D.J. Perreault, "Evaluation of magnetic materials for very high frequency power applications," *IEEE Transactions on Power Electronics*, vol. 27, no. 1, pp. 425-435, Jan. 2012.

[22] J-P. Keradec, B. Cogitore and F. Blache, "Power transfer in a two-winding transformer: from 1-D propagation to an equivalent circuit," *IEEE Transactions on Magnetics*, vol. 32, no. 1, pp. 274-280, Jan. 1996.

[23] A. Schellmanns, P. Fouassier, J.-P. Keradec, J.-L. Schanen, "Equivalent circuits for transformers based on one-dimensional propagation: accounting for multilayer structure of windings and ferrite losses," *IEEE Transactions on Magnetics*, vol. 36, no. 5, pp. 3778-3784, Sept. 2000.

[24] R.W. Erickson and D. Maksimovic, "A multiple-winding magnetics model having directly measurable parameters," *Proceedings of the IEEE Power Electronics Specialists Conference (PESC)*, vol. 2, pp. 1472-1478, 17-22, May 1998.

[25] A. Schellmanns, K. Berrouche, and J.-P. Keradec, "Multiwinding transformers: a successive refinement method to characterize a general equivalent circuit," *IEEE Transactions on Instrumentation and Measurement*, vol. 47, no. 5, pp. 1316-1321, Oct. 1998.

[26] J.M. Lopera, M. Pernia, J. Diaz, J.M. Alonso and F. Nuno, "A complete transformer electric model, including frequency and geometry effects," *Proceedings of the IEEE Power Electronics Specialists Conference (PESC)*, vol. 2, pp. 1247 - 1252, June 1992.

[27] A.M. Pernia, F. Nuno and J.M. Lopera, "Magnetic elements simulation in power converters," *Technical Proceedings of the International Power Electronics Congress (CIEP)*, pp.74-79, 21-25 Aug. 1994.

[28] A.M. Pernia, F. Nuno and J.M. Lopera, "1D/2D transformer electric model for simulation in power converters," *Proceedings of the IEEE Power Electronics Specialists Conference (PESC)*, pp.1043-1049 vol.2, 18-22, Jun 1995.

[29] R. Prieto, J.A. Cobos, O. Garcia, P. Alou and J. Uceda, "Using parallel windings in planar magnetic components," *Proceedings of the IEEE Power Electronics Specialists Conference (PESC)*, pp. 2055-2060, vol. 4, 2001.

[30] J.M. Lopera, M.J. Prieto, A.M. Perna, and F.N. Nuno, "A Multiwinding Modeling Method for High Frequency Transformers and Inductors," *IEEE Transactions on Power Electronics*, vol. 18, no. 3, May 2003.

[31] R. Prieto, J.A. Oliver, J.A. Cobos, and M. Christini, "Magnetic Component Model for Planar Structures Based on Transmission Lines," *IEEE Transactions on Industrial Electronics*, vol. 57, no. 5, May 2010.

[32] W. Chen, Y. Yan, Y. Hu and Q. Lu, "Model and design of PCB parallel winding for planar transformer," *IEEE Transactions on Magnetics*, vol. 39, no. 5, pp. 3202-3204, Sept. 2003.

[33] X. Margueron and J-P. Keradec, "Design of Equivalent Circuits and Characterization Strategy for n-Input Coupled Inductors," *IEEE Transactions on Industry Applications*, vol. 43, no. 1, pp. 14-22, Jan.-Feb. 2007.

[34] X. Margueron, A. Besri, Y. Lembeye and J.-P. Keradec, "Current sharing between parallel turns of a planar transformer: prediction and improvement using a circuit simulation software," *IEEE Transactions on Industry Applications*, vol. 46, no. 3, May-Jun. 2010.

[35] Z. Ouyang, O.C. Thomsen, and M. Andersen, "Optimal Design and Tradeoff Analysis of Planar Transformer in High-Power DCDC Converters," *IEEE Transactions on Industrial Electronics*, vol.59, no.7, pp.2800-2810, July 2012.

[36] MIT EE Staff, "Transformers; General Principles," in *Magnetic Circuits and Transformers*, Cambridge, MA: The MIT Press, 1943.

[37] H.A. Haus and J.R. Melcher, "Introduction to Electroquasistatics and Magnetoquasistatics", in *Electromagnetic Fields and Energy*, Englewood Cliffs, NJ: Prentice-Hall, 1989.

[38] J.G. Kassakian, M.F. Schlecht and G.C. Verghese, "Magnetic Components," in *Principles of Power Electronics*, Addison-Wesley, 1991.

[39] R.W. Erickson and D. Maksimovic, "Basic Magnetics Theory," in *Fundamentals of Power Electronics*, Boston, MA, USA: Kluwer, 2001.

[40] J.G. Hayes, N. O'Donovan, and M.G. Egan, "The extended T model of the multiwinding transformer," *Proceedings of the IEEE Power Electronics Specialists Conference*, pp. 1812-1817, Vol. 3, 20-25 June 2004.

[41] C.P. Schultz, "The Coupled Leakage Model of a multiple winding transformer," *Proceedings of IEEE Southeastcon*, pp. 6-11, Mar. 2011.

[42] V.A. Niemela, G.R. Skutt, A.M. Urling, Y.-N. Chang, T.G. Wilson, Jr. H.A. Owen, and R.C. Wong, "Calculating the short-circuit impedances of a multiwinding transformer from its geometry," *Proceedings of the IEEE Power Electronics Specialists Conference (PESC)* pp. 607-617, vol. 2, 26-29 Jun. 1989.

[43] C.R. Sullivan and R.Y. Zhang, "Simplified design method for litz wire," *Proceedings of the IEEE Applied Power Electronics Conference and Exposition (APEC)*, pp.2667-2674, 16-20 March 2014.

[44] J. Hu and C.R. Sullivan, "AC resistance of planar power inductors and the quasidistributed gap technique," *IEEE Transactions on Power Electronics*, vol.16, no.4, pp.558-567, Jul 2001.